International Journal of Pharmaceutics 688 (2026) 126440

Contents lists available at ScienceDirect

International Journal of Pharmaceutics

journal homepage: www.elsevier.com/locate/ijpharm

Emulsion-Solvent diffusion in a double-chip microfluidic platform for scalable production of Lipid@PLGA nanoparticles delivering siRNA therapeutics

Ersilia Villano [a], Teresa Silvestri [a], Susy Brusco [a], Erika Esposito [a], Chiara Infolfi [a], Thomas L. Moore [a], Emma Mitidieri [a], Raffaella Sorrentino [a], Fabiana Quaglia [a], Paola Brocca [b], Ivana d'Angelo [c], Roberta d'Emmanuele di Villa Bianca [a], Gabriella Costabile [a,*], Francesca Ungaro [a]

[a] Department of Pharmacy, University of Napoli Federico II, Napoli 80131, Italy
[b] Department of Medical Biotechnologies and Translational Medicine, University of Milano, Segrate 20090, Italy
[c] Di.S.T.A.Bi.F., University of Campania Luigi Vanvitelli, Caserta 81100, Italy

ARTICLE INFO

Keywords:
Microfluidic
Nanoparticles fabrication
Hybrid Lipid Polymer Nanoparticles
PLGA
siRNA
NF-kB

ABSTRACT

Scalable nanoparticle manufacturing remains a key bottleneck in the clinical translation of RNA-based nanomedicines. In this study, we demonstrate the successful adaptation of a conventional emulsion–solvent diffusion protocol into an automated microfluidic workflow, illustrating its potential for streamlined and scalable nanoparticle production. Using the Sunshine™ microfluidic platform (Unchained Labs), we systematically optimized formulation and process parameters to produce siRNA-loaded hybrid lipid–polymer nanoparticles, featuring a poly(lactic-co-glycolic acid) (PLGA) core and a dipalmitoylphosphatidylcholine shell (*m*DPPC@PLGA hNPs). Optimised *m*DPPC@PLGA hNPs exhibited key technological features, matching or exceeding the quality of their benchtop equivalents (*b*DPPC@PLGA hNPs). Using poly(vinyl alcohol) (PVA) as a stabilizer, monodisperse *m*DPPC@PLGA hNPs with controlled size (<170 nm) and consistent zeta potential (–30 mV) were achieved with production yields ≥ 40 %. The ability of *m*DPPC@PLGA hNPs to effectively entrap and slowly release a siRNA targeting nuclear factor NF-κB (siNFκB) was successfully demonstrated. Structural characterization through thermodynamic and SAXS analyses confirmed that the microfluidic produced hNPs retained comparable internal architecture to their benchtop counterparts. Most notably, siNFκB-loaded *m*DPPC@PLGA hNPs resulted in effective *in vitro* downregulation of NFκB in lipopolysaccharide-stimulated A549 lung epithelial cells. Collectively, these results establish a novel and robust approach for the scalable fabrication of functional, siRNA-loaded hybrid nanoparticles via emulsion–solvent diffusion, leveraging a commercially available, automated microfluidic system with a serial chip configuration.

1. Introduction

The rapid advancement of the RNA therapeutic field has been driven by innovations in core technologies, including RNA synthesis, chemical modifications, and delivery strategies (Liu et al., 2025a; Sun et al., 2024; Wang et al., 2025). In the specific context of lung delivery of short interference RNAs (siRNA), our research group has designed hybrid core–shell nanoplatforms, consisting of a poly(lactide-co-glycolide) (PLGA) core surrounded by a lipid shell (Lipid@PLGA hNPs) (Brusco et al., 2024; Comegna et al., 2021; Conte et al., 2022; d'Angelo et al., 2018). The results highlight the strong potential of dipalmitoyl phosphatidylcholine (DPPC)-engineered hNPs (DPPC@PLGA hNPs), successfully developed *via* emulsion–solvent diffusion, as efficient carriers for siRNA delivery in the local treatment of pulmonary diseases (Comegna et al., 2021; Conte et al., 2022; d'Angelo et al., 2018). Nonetheless, the growing demand for RNA-based nanomedicines for clinical applications underscores the urgent need to strengthen the manufacturing capacity of this nanoplatform in the industrial setting.

The transition from laboratory-scale processes to large-scale manufacturing poses significant challenges, including the need to

* Corresponding author.
E-mail address: gabriella.costabile@unina.it (G. Costabile).

https://doi.org/10.1016/j.ijpharm.2025.126440
Received 10 September 2025; Received in revised form 26 November 2025; Accepted 27 November 2025
Available online 5 December 2025

maintain batch-to-batch consistency in terms of Critical Quality Attributes (CQAs), product stability, and preservation of therapeutic efficacy (Germain et al., 2020; Joyce et al., 2024; Wang and Song, 2017). For RNA nanomedicines, industrial manufacturing presents additional regulatory complexities, primarily due to the intrinsic variability of biological materials and the use of sophisticated technologies that hinder scalability and reproducibility (Liu et al., 2025b). Therefore, simplifying and standardizing all stages of RNA nanoplatform production is essential. This requires the adoption of advanced technologies capable of ensuring quality, safety, and regulatory compliance throughout the entire product lifecycle (Joyce et al., 2024; Zhang et al., 2025).

Although the emulsion–solvent diffusion technique offers significant advantages for encapsulating sensitive macromolecular drugs (e.g., RNA therapeutics) within biodegradable polymer matrices under mild processing conditions, several challenges remain. Emulsifying large volumes of liquid in industrial settings can be a complex task; it is time-consuming and requires emulsification techniques that differ from those used in lab-scale probe sonication or magnetic stirring (e.g., high-shear homogenizers, rotor–stator systems, and high-pressure homogenization). Though scalable in principle, the transition from lab-scale to industrial production requires careful control over process parameters to ensure batch consistency and compliance with regulatory standards (Hernández-Giottonini et al., 2020). Emulsion stability is a critical factor, as variations in stabilizer type and concentration, mixing intensity, and diffusion rates can affect nanoparticle uniformity and drug loading.

Although several scale-independent processes have been previously reported, such as focused ultrasound (Schiller et al., 2015), spray drying (Schiller et al., 2020), spinning disc evaporation-triggered nanoprecipitation (Zander et al., 2025), microtemplating techniques (Kronenfeld et al., 2024) via microfluidics (Roces et al., 2020), the formation of a PLGA core covered with a phospholipid shell requires specific considerations during the self-assembly process. Microfluidics has recently emerged as a promising approach to overcoming these challenges by providing enhanced control over key process parameters for nanoparticle fabrication. As a result, it significantly influences the key attributes of the resulting nanoplatforms at large scale, including size, polydispersity, morphology, encapsulation efficiency, and batch-to-batch reproducibility (Shepherd et al., 2021). Indeed, microfluidic platforms provide: i) rapid and controlled mixing at the microscale, producing monodisperse nanoparticles with minimal batch-to-batch variability; ii) adaptable microchannel geometries and architectures for improved drug loading efficiency and colloidal stability; iii) scalability for industrial-level manufacturing and increased production throughput. Here, using two microfluidic chips in series enables control over both the initial formation of PLGA nanoparticles and the subsequent post-functionalization of their surfaces with the lipid, which would be harder to achieve with other scalable methods.

The literature reports several examples of emulsification methods being transitioned to microfluidic systems (Li et al., 2025; Wadhwa et al., 2023), although these are often implemented using custom-built, lab-scale devices and chips. A successful, scalable transition ensures the standardization, reproducibility, and reliability of the generated knowledge. With a particular focus on increasing the translational potential of the developed lipid@PLGA hybrid nanoplatforms for siRNA delivery, this work aims to advance toward a continuous, scalable manufacturing process. Specifically, the emulsion–solvent diffusion protocol previously published to produce DPPC@PLGA hNPs was adapted from the lab bench to an automated microfluidic platform equipped with a double-chip-in-series system. Formulation and process parameters were systematically changed to obtain DPPC@PLGA hNPs by microfluidics (*m*DPPC@PLGA hNPs), matching the quality attributes of previously optimised hNPs prepared by benchtop emulsion-solvent diffusion (*b*DPPC@PLGA hNPs). The ability of optimised *m*DPPC@PLGA hNPs to encapsulate and to slowly release a siRNA pool targeting nuclear factor NF-κB (siNFκB) was successfully demonstrated. To gain further insights into the chemical structure of hNPs produced via microfluidic techniques, thermal analysis and Small-Angle X-ray Scattering (SAXS) were performed. Finally, preliminary *in vitro* studies confirmed the gene silencing efficacy of the formulation in a lipopolysaccharide (LPS)-stimulated human lung epithelial cell model (A549) overexpressing NF-κB.

2. Materials and methods

2.1. Materials

Poly(D, L-lactide-co-glycolide) (PURASORB® 5002A, PLGA 50:50 acid-terminated, inherent viscosity 0.16–0.24 dL/g) was purchased from PolySciTech (West Lafayette, IN, USA). 1,2-Dipalmitoyl-*sn*-glycero-3-phosphocholine (DPPC) was kindly gifted from Lipoid GmbH (Steinhausen, ZG, CH). Dharmacon™ ON-TARGETplus™ siRNA pools against p50 (SMARTpool NfkB1 siRNA) and p65 (SMARTpool RelA siRNA) NF-kB subunits in a 1:1 ratio, and ON-TARGETplus™ non-targeting siRNA pool (*scrambled* siRNA or siNC) was purchased from Carlo Erba Reagents s.r.l. (Milano, IT). Resomer® RG 502H (PLGA 50:50 acid-terminated, inherent viscosity 0.16–0.24 dL/g), Polyvinyl alcohol (PVA; Mowiol® 4–88, Mw 31,000 g/mol; degree of hydrolysis 86.7–88.7 %), Phosphotungstic acid hydrate, dichloromethane (DCM), and ethanol 96 % (v/v) were purchased from Sigma-Aldrich (St. Loouis, MO, USA). Quant-IT RiboGreen reagent and UltraPure™ distilled water DNase/RNase-free were purchased from Life Technologies (Carlsbad, CA, USA). 3D Flow Focusing Chip 100 μm (Hydrophobic) (3200434), Droplet Junction Chip 100 μm (Hydrophilic) (3000158), and 190 μm (Hydrophilic) (3200155) were purchased from Dolomite Microfluidics – Unchained Labs (Pleasanton, CA, USA).

2.2. Microfluidic production of DPPC@PLGA hNPs

DPPC@PLGA hNPs were manufactured by the microfluidic hydrodynamic focusing approach using the automated nanoparticle system Sunshine™ (Unchained Labs). To transition to the emulsion-solvent diffusion technique, a double-chip setup was used in series, with the first chip reproducing the W/O emulsion and the second simulating the solvent diffusion phase. Three different chips with an X-junction configuration were evaluated (i.e., Droplet Junction Chip 100 μm, Droplet Junction Chip 190 μm, and 3D Flow focusing 100 μm) for their contribution to particle formation.

The organic phase (O) was prepared by solubilizing different amounts of PLGA (0.5 %, 1 %, and 5 % w/v) and 0.5 mg/mL DPPC (1:20 w/w DPPC: PLGA) in DCM. For the aqueous phase (W), RNase-free water was used. When siRNA-loaded DPPC@PLGA hNPs were produced, siRNA was added to W at different theoretical loading amounts (0.2 nmol or 1 nmol/10 mg PLGA, respectively DPPC@PLGA_siNFkB_0.2 and DPPC@PLGA_siNFkB_1).

The emulsion is formed in the first chip, where W flows through the inner channel via a linear connector tube, while DCM flows through the outer channel *via* a T-connector. At the exit of the first chip, the emulsion (W/O) is collected and forced through a connection into the second chip, where it flows as the inner phase. In contrast, ethanol, used as a diffusion solvent (D), flows in the outer channel through a T-connector tube. The impact of different production parameters was tested, namely total flow rates (TFRs) (1, 1.5, 3, and 6 mL/min) and flow rate ratios (FRR) (W:O:D 5:1:10, 1:2:10, and 1:3:10). At the exit of the second chip, the resulting dispersion was added dropwise into water, which served as the diluting phase (DL). The effect of polyvinyl alcohol (PVA) 4–88 added as a stabilizing agent in the DL was evaluated at different weight ratios relative to PLGA: 0, 1:2, 1:4, 1:6, and 1:8 (w/w).

The hNP dispersion is collected and kept under magnetic stirring for 10 min before proceeding with the removal of residual solvent by rotary evaporation under vacuum at 30 °C (Heidolph VV 2000, Germany). The hNPs dispersion was then centrifuged at 9500 rcf for 20 min at 4 °C and brought to a final concentration of 20 mg/mL with RNase-free water.

As a benchtop reference formulation, *b*DPPC@PLGA hNPs were produced using the conventional emulsion–solvent diffusion technique, as previously described by our laboratory (Conte et al., 2022; d'Angelo et al., 2018).

2.3. Characterization of DPPC@PLGA hNPs

2.3.1. Colloidal properties

The hydrodynamic diameter (D_H) and the polydispersity index (PDI) of hNPs were determined by DLS, with a Malvern Zetasizer Nano ZS (Malvern Instruments). Samples were diluted in ultra-purified water (UPW) to achieve an attenuator setting between 6 and 8. Results are expressed as mean value ± standard deviation (SD) of three independent batches. The zeta potential (ζ potential) of hNPs was determined by electrophoretic light scattering (ELS) with a Zetasizer Nano ZS (Malvern Instruments Ltd, UK) after diluting the samples 1:100 with UPW. Results are expressed as mean value ± standard deviation (SD) of three independent batches.

2.3.2. Yield of production

The yield of the particle production process was evaluated after the whole batch of particles was freeze-dried at the end of the process. The yield is defined as the percentage ratio of the mass of particles collected to the theoretical mass of material initially processed during particle production (Eq. 1).

$$\%\ Yield\ of\ Production = \frac{Collected\ amount\ of\ hNPs}{Theoretical\ amount\ of\ hNPs} \times 100$$

In all cases, results are reported as the mean of three measurements across three batches (n = 9) ± standard deviation (SD).

2.3.3. Comparative statistical analysis

To identify the formulation that best reproduced the quality attributes of the reference *b*DPPC@PLGA hNPs, a statistical comparison was performed across four nanoparticle attributes: size, PDI, zeta potential, and production yield. Statistical analysis was performed using *R* version 4.4.3. First, the difference in means between each attribute was performed via a post-hoc Tukey's Honestly Significant Difference (Tukey's HSD) test. Subsequently, only those microfluidic formulations that were not significantly different from the benchtop formulation (p-value > 0.05) were selected. All microfluidic formulations differed significantly in their production yields; therefore, all formulations were considered in the latter calculations to identify the one with the highest similarity to *b*DPPC@PLGA hNPs. For each attribute, the relevant microfluidic formulations subset, and the absolute difference between the microfluidic attribute (e.g., size, PDI, zeta potential, % yield) and the benchtop attribute was calculated (Eq. 2):

$$\delta_{i,j} = \left|\overline{x}_{i,j,microfluidic} - \overline{x}_{i,benchtop}\right|$$

where $\delta_{i,j}$ is the absolute difference of the mean of attribute i for formulation j produced via microfluidics ($\overline{x}_{i,j,microfluidics}$) and $\overline{x}_{i,benchtop}$ is the mean of that attribute produced via the benchtop method. A smaller δ indicates a small difference between the benchtop and microfluidic formulation.

A score was then calculated for each attribute based on the percentage of the absolute difference over the max–min range of that attribute for all formulations (Eq. 3):

$$Score_i = 100 \cdot \left(1 - \frac{\delta_{i,j} - \delta_{i,min}}{\delta_{i,max} - \delta_{i,min}}\right)$$

where $Score_i$ is the score for attribute i, $\delta_{i,max}$ is the maximum average absolute difference of attribute i between all microfluidic formulations and the standard benchtop formulation, and $\delta_{i,min}$ is the corresponding minimum. A score of 100 % represents the best outcome, indicating the smallest difference between the microfluidic and benchtop formulations. This approach was chosen to better reflect the magnitude of differences across formulations by leveraging the max–min range, as opposed to relying solely on a simple rank ordering from worst to best.

2.4. siRNA encapsulation efficiency and heparin displacement assay

The loading efficiency of siRNA in the hNPs was evaluated using an indirect method, as previously described (Conte et al., 2022; d'Angelo et al., 2018). Briefly, DPPC@PLGA hNPs are centrifuged at 9500 rcf for 20 min at 4 °C. The amount of siRNA remaining in the supernatant after centrifugation was quantified using the Quant-iT™ RiboGreen® RNA assay kit (Thermo Fisher, Waltham, MA, USA) according to the manufacturer's instructions, and the derivatized samples were analyzed with a GloMax plate reader (Promega Corporation, Madison, WI, USA). Results are reported as actual loading (nmol of encapsulated siRNA per mg of hNPs based on the yield of production) and encapsulation efficiency (actual loading/theoretical loading × 100) ± SD of values collected from three different batches.

Moreover, after production and indirect evaluation of encapsulation efficiency, the heparin displacement assay was performed on the siRNA-loaded hNPs to assess the amount of siRNA adsorbed on the surface relative to the amount effectively encapsulated within the PLGA core. Thus, the hNPs were washed with a heparin solution (at a 200-fold molar excess relative to the encapsulated siRNA) and incubated at 37 °C for 30 min. Following centrifugation, the siRNA collected into the supernatant was quantified using the Quant-iT RiboGreen RNA assay kit, as previously described.

2.5. Nanoparticle Tracking analysis (NTA)

The size distribution and concentration in water of siRNA-loaded DPPC@PLGA hNPs were also determined by NTA using a NanoSight Pro system (Malvern Panalytical, Malvern, UK) configured with a 488 nm laser and a high-sensitivity scientific CMOS camera. Samples were diluted to an acceptable concentration to obtain an optimal range of 20–150 particles/frame. Samples were analyzed under constant flow conditions (flow rate = 2 µl/min) at 25 °C (Tian et al., 2024). For each sample, 5 videos of 60″ duration were recorded, and data were processed using NS Xplorer software (Malvern Panalytical, Malvern, UK). Post-acquisition settings were kept constant between samples. The data obtained were particle concentration (particles/mL), average size (nm), and particle size distribution (SPAN), and have been expressed as the mean value ± standard deviation (SD) of three independent batches.

2.6. Transmission electron microscopy (TEM)

The morphology of the optimized siRNA-loaded DPPC@PLGA hNPs was evaluated by TEM with a FEI™ Tecnai G2 S-TWIN microscope equipped with a FEI™ Eagle 4 K camera. Sample analysis was performed on air-dried 7 µL hNPs dispersions in water (10 mg/mL) mounted on 200-mesh copper grids coated with carbon film (Ted Pella Inc., Nanovision, Brugherio, IT). Before analysis, the NPs were stained with 0.2 µm filtered phosphotungstic acid (1 % w/v, pH = 7).

2.7. Differential scanning calorimetry (DSC)

A differential scanning calorimeter (Q20, TA Instruments, USA) was used for thermoanalytical testing. Hermetic T_{zero} aluminum sealed pans containing precisely weighed solid samples (~4 mg) were heated from 10 to 250 °C at a constant heating rate of 5 °C/min. Measurements were performed under an inert nitrogen atmosphere, purged at 50 mL/min, using an empty pan as a reference. The thermodynamic properties, such as melting temperature (Tm), decomposition, and glass transition temperature (Tg), of *m*DPPC@PLGA_siNFkB_0.2 hNPs were analyzed and compared to those of all the required controls, including

*b*DPPC@PLGA_siNFkB_0.2 hNPs, unloaded *m*DPPC@PLGA, and *b*DPPC@PLGA, as well as the raw materials (i.e., PLGA and DPPC). The hNPs samples were all freeze-dried for 24 h (0.1 mbar, −80 °C) using a Lyovapor L-200 laboratory freeze-drier (BUCHI Italia s.r.l, Cornaredo, Italy). The thermograms were evaluated using the TA-Universal Analysis software.

2.8. SAXS analysis

Small-angle X-ray scattering (SAXS) measurements were performed at the Id02 beamline of the ESRF synchrotron facility in Grenoble (FR). Samples were prepared from an initial hNP dispersion in water (10 mg/mL). A Eiger2 4 M detector was used at two different sample-to-detector distances of 10 and 1 m to cover the direct space interval of approximately 1 μm to approximately 1 nm, with profitable overlapping. Flow through glass cells was used. Empty capillaries and capillaries filled with water have been measured in the same conditions, for background subtraction. SAXS data were acquired for *m*DPPC@PLGA_siNFkB_0.2 and *b*DPPC@PLGA_siNFkB_0.2, and the scattering profiles were treated by applying the stabilization method. The scattering profiles were then treated using SAXS utilities software (Michael, 2021). Data were analyzed with the SasView fitting software (Breßler et al., 2015) (https://www.sasview.org/) employing a core–shell sphere_sld form factor combined with a 'sticky' hard-sphere structure factor (Kotlarchyk and Chen, 1983; Menon et al., 1991). SAXS was also applied to dispersions of the same particles in artificial mucus (AM) at three different volume ratio, namely 1:1, 2:1, and 3:1 v/v. AM was prepared as previously reported (Brusco et al., 2024; Costabile et al., 2015). Briefly, 25 μL of sterile egg yolk emulsion, 25 mg of mucin from porcine stomach, Type II, 20 mg of DNA, 30 μL of aqueous DTPA (1 mg mL − 1), 25 mg NaCl, 11 mg KCl, and 100 μL of RPMI 1640 were added to 5 mL of water, and the dispersion was stirred until a homogenous mixture was obtained.

2.9. In vitro release kinetics

Release studies were performed on hNP dispersions in phosphate-buffered saline (PBS, 120 mM NaCl, 2,7 mM KCl, 10 mM phosphate salt, pH = 7.4) at 37 °C. Briefly, 10 μL of siRNA-loaded hNPs were diluted in PBS to reach a final concentration of 0.02 nmol/mL and incubated in a shaking water bath (ShakeTemp SW 22, Julabo Italia S.r.l., Padova, Italy) at 37 °C. At scheduled time points, the samples were centrifuged, and 800 μL of supernatant was analysed for siRNA concentration using the Quant-IT RiboGreen reagent kit as reported above. Then, the pellet was resuspended in fresh media to reach a final volume of 1 mL and incubated in a thermostat-shaking water bath for the following time points.

2.10. In vitro NF-κB gene silencing

2.10.1. Cell culture

Human lung adenocarcinoma epithelial cells (A549) were cultured in RPMI-1640 medium (Invitrogen s.r.l., Monza Italy) supplemented with 10 % fetal bovine serum (FBS), 1 % L-glutamine, and 1 % penicillin–streptomycin. Cells were maintained at 37 °C in a humidified incubator with 5 % CO_2 and 90 % relative humidity. Upon reaching confluence, cells were detached using trypsin and seeded into 6-well plates at a density of 2.5 × medium 10^5 cells/well in 2 mL of the same RPMI medium supplemented with the same additives.

2.10.2. In vitro NF-κB gene silencing in LPS-stimulated A549 cells

Cells were allowed to adhere and grow for 24 h under standard culture conditions. A preliminary cytotoxicity assay was carried out on A549 cells by MTT [3-(4,5-dimethylthiazol-2-yl) 2,5-diphenyltetrazolium bromide] assay after treatment with *m*DPPC@PLGA_hNPs (0.05, 0.1, and 0.2 mg/mL) for 24 h and 48 h (Esposito et al., 2024). To test the NF-kB gene silencing *in vitro*, A549 cells were treated with *m*DPPC@PLGA_siNFkB hNPs or *b*DPPC@PLGA_siNFkB hNPs carrying 40 nM siRNA targeting NF-κB (siNFκB) corresponding to 0.2 mg/mL of DPPC@PLGA_siNFκB_1, at 37 °C in a humidified atmosphere containing 5 % CO_2. At 42 h, cells were stimulated with LPS (10 μg/mL) to induce NF-κB expression, and the incubation was stopped at 48 h. Transfection using siRNA/lipofectamine complexes served as a positive control (Fig. 1).

2.10.3. Western Blot

The cells were lysed in RIPA buffer supplemented with a 1 × protease and phosphatase inhibitor cocktail (Sigma, Italy) (d'Emmanuele Di Villa Bianca et al., 2010). Protein expression levels of the NFκB p65 subunit were assessed by using a primary antibody (1:1000, Cell Signaling, MA, USA). Membranes were washed thoroughly with PBS containing 0.1 % (v/v) Tween-20, then incubated with horseradish peroxidase (HRP)-conjugated secondary antibodies for 2 h at room temperature. After final washes, protein bands were visualized using the ChemiDoc Imaging System (Bio-Rad Laboratories, Hercules, CA, USA). Protein levels were normalized to β-actin expression (1:3000, Thermo Fisher, Waltham, MA, USA).

Data are presented as mean ± standard error (SEM), n = 4. Statistical analysis was conducted using one-way ANOVA followed by Bonferroni post hoc test, with significance levels set at °$p < 0.05$ vs. CTR, and *$p < 0.05$, **$p < 0.01$ vs. CTR and *$p < 0.05$, **$p < 0.01$ vs. LPS.

3. Results and discussion

3.1. Transitioning bench-top DPPC@PLGA hNPs production in microfluidic

Our previous work focused on optimizing formulation components and process parameters to develop hybrid nanoparticles comprising a PLGA core and a dipalmitoylphosphatidylcholine lipid shell (DPPC@PLGA hNPs), meeting quality attributes for pulmonary delivery of siRNA — namely, controlled particle size, low polydispersity, defined morphology, high encapsulation efficiency, and favourable release kinetics (Conte et al., 2022; d'Angelo et al., 2018). To fully exploit the potential of this nanoplatform, the present study translates the production of DPPC@PLGA hNPs *via* emulsion–solvent diffusion from a benchtop (Fig. 2A) to an automated manufacturing technique *via* a commercially available microfluidic platform (Sunshine™, Unchained Labs) (Fig. 2B-C).

A setup incorporating two chips in series was specifically developed. The aim was to replicate the water-in-oil (W/O) emulsion step in the first chip, followed by the hNP precipitation into the diffusion phase (D) in the second chip. Formulation and process parameters were systematically changed to obtain DPPC@PLGA hNPs produced *via* microfluidic (*m*DPPC@PLGA hNPs) matching or exceeding the quality attributes of the previously optimized benchtop-produced hNPs (*b*DPPC@PLGA). Thus, after production, *m*DPPC@PLGA hNPs were characterized for colloidal properties and yield of production and results compared to *b*DPPC@PLGA hNPs.

The impact of the chip coating on the particle formation process was first assessed by connecting a 190 μm chip with a X-junction configuration to a 100 μm chip with a X-junction configuration, both of which were internally coated with a hydrophilic material (Fig. 2B). While the PLGA concentration (% w/v) and flow rate ratio (FRR) were kept constant, the total flow rate (TFR) was varied (i.e., 1.5, 3.0, 5.0, and 6.0 mL/min) as detailed in Table S1. Notably, the results obtained under these conditions do not align with the desired target characteristics (Table S1). Operating with two hydrophilic chips in series requires the system to operate at an FRR that favours the W phase. This, in turn, reduces the proportion of the O phase (DCM) and, consequently, the amount of PLGA available for hNP formation. As a result, both the production yield and the colloidal features of the *m*DPPC@PLGA hNPs are significantly compromised.

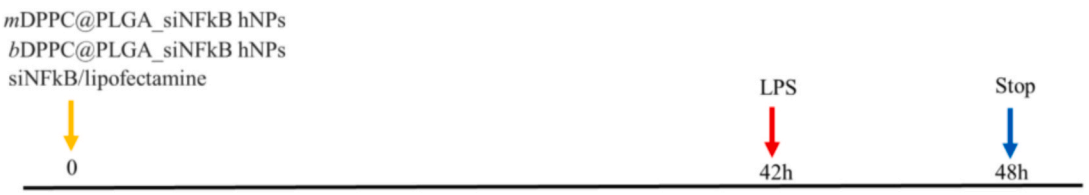

Fig. 1. Experimental plan for cell treatment.

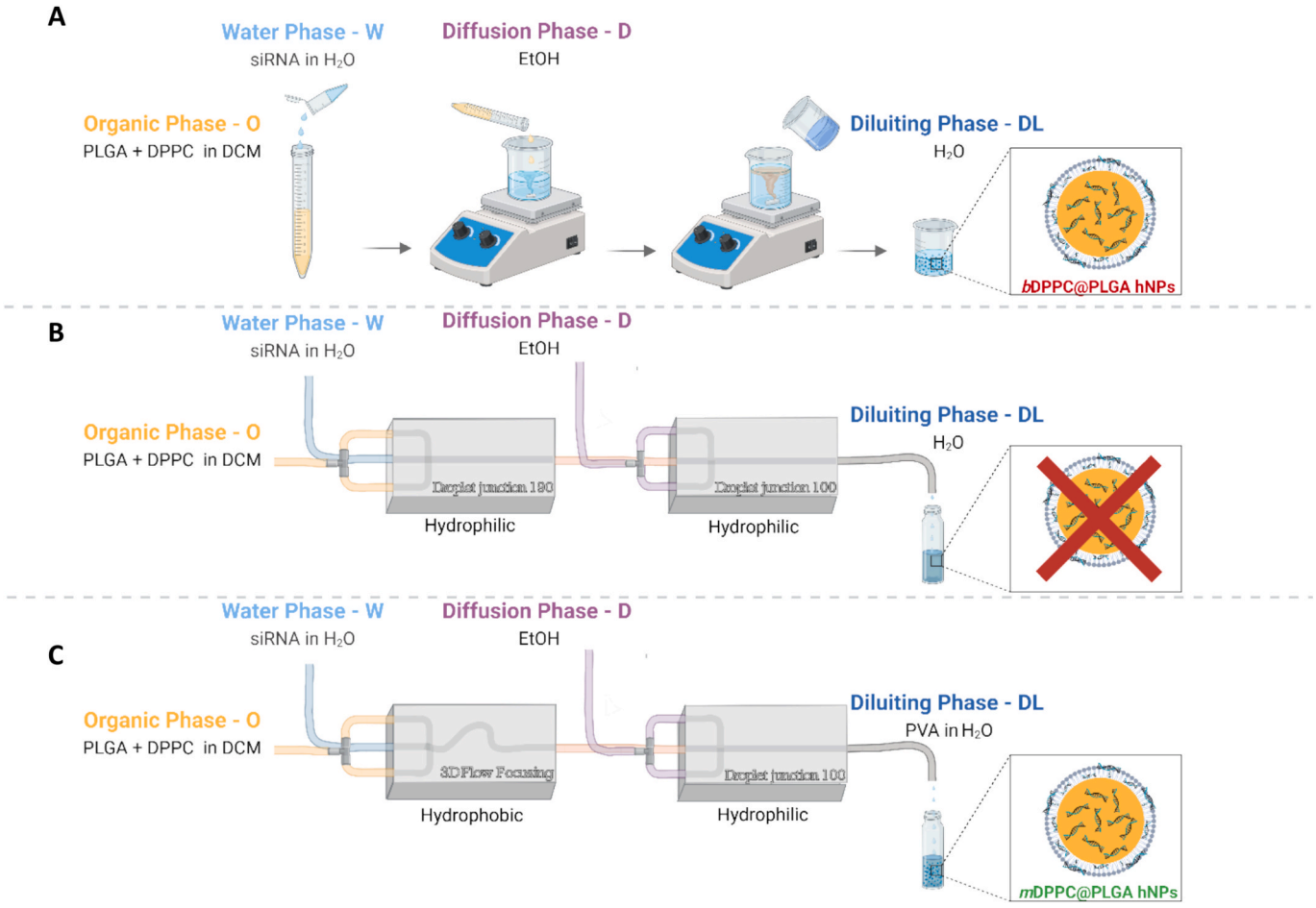

Fig. 2. Schematic representation of the preparation of siRNA-loaded DPPC@PLGA hNPs by benchtop emulsion-solvent diffusion technique (A) in comparison to the double chip microfluidic manufacturing (B-C). The optimized protocol is depicted in panel C.

Based on these preliminary data, the chip setting was modified to include a hydrophobic coating, which improves compatibility with the PLGA-containing organic solvent (i.e., DCM). Furthermore, the 2D geometry was replaced with a 3D flow focusing chip, which has been shown to improve polymer separation from channel walls during the hNP formation process (Shepherd et al., 2021; Unchained Labs, 2024). The new two-chip-in-series configuration comprised the 3D flow focusing chip with a hydrophobic coating, followed by the 100 μm hydrophilic chip with an X-junction configuration (Fig. 2C).

Using this configuration, the formulation study explored PLGA concentrations ranging from 1 % to 5 % w/v, combined with TFRs ranging from 1.5 to 6.0 mL/min, and two different FRRs (2:1:10 and 3:1:10) (Table 1). Again, all formulations were characterized for their colloidal properties and production yield, and the results were compared with those of the reference *b*DPPC@PLGA hNPs. The collected results clearly confirm the key role of PLGA concentration in achieving monodisperse hNPs, while highlighting that a low TFR and a high FRR ensure better control over both PDI and production yield (Table 1). As reported by manufacturers, a lower polymer concentration enables the formation of smaller droplets and, consequently, smaller particles (Unchained Labs, 2024). Conversely, highly concentrated PLGA solutions become increasingly viscous, thereby affecting droplet formation. In fact, across all tested conditions, 5 % PLGA concentrations led to undetectable production yields, with PDI values ranging from 0.25 ± 0.02 (m12) to 0.38 ± 0.08 (m17), indicating poor nanoparticle formation and high particle-size variability.

At the intermediate PLGA concentration tested of 1 % w/v, the production yield slightly improves, reaching values ranging between 15.2 ± 2.1 % (*m*3) and 9.6 ± 2.3 % (*m*12). Nevertheless, acceptable PDI values were never achieved. This still indicates an overall heterogeneous particle population across all tested FRR and TFR conditions. The most effective conditions are associated with *m*1, where maintaining low values for both PLGA concentration and TFR (i.e., 1.5 mL/min), along with a slightly higher FRR (2:1:10), enabled the formation of DPPC@PLGA hNPs *via* microfluidics. This formulation was further demonstrated to be statistically the most similar overall to the reference

Table 1
Effect of PLGA amount (% w/v), total flow rate (TFR), and Flow rate ratio (FRR) on the colloidal properties of *m*DPPC@PLGA hNPs. Colloidal properties of *b*DPPC@PLGA are reported in comparison. Results are reported as mean ± standard deviation (SD) from three independent batches (n = 3).

Formulation	PLGA % w/v	TFR mL/min	Water Phase	Organic Phase	Diffusion Phase	D_H (nm ± SD)	PDI (mean ± SD)	ζ potential (mV ± SD)	YP (% ± SD)
*b*DPPC@PLGA	1	–	–	–	–	159.7 ± 2.1	0.14 ± 0.02	−28.4 ± 2.4	54.5 ± 4.3
*m*1	0.5	1.5	1	2	10	166.5 ± 19.9	0.21 ± 0.08	−28.7 ± 5.9	37.1 ± 2.7
m2	0.5	1.5	1	3	10	257.2 ± 13.8	0.29 ± 0.11	−37.4 ± 4.2	36.8 ± 2.4
m3	1	1.5	1	2	10	225.3 ± 27.2	0.28 ± 0.05	−26.5 ± 5.9	15.2 ± 2.1
m4	1	1.5	1	3	10	301.6 ± 5.1	0.27 ± 0.02	−27.5 ± 3.5	13.3 ± 4.1
m5	5	1.5	1	2	10	183.2 ± 12.3	0.31 ± 0.10	−26.5 ± 5.9	–
m6	5	1.5	1	3	10	163.9 ± 23.4	0.33 ± 0.01	−27.5 ± 3.5	–
m7	0.5	3.0	1	2	10	313.1 ± 22.9	0.29 ± 0.10	−29.9 ± 1.5	35.3 ± 2.4
m8	0.5	3.0	1	3	10	141.7 ± 17.3	0.25 ± 0.07	−30.8 ± 2.8	34.3 ± 2.3
m9	1	3.0	1	2	10	174.6 ± 28.4	0.27 ± 0.03	−24.7 ± 4.2	10.3 ± 1.8
m10	1	3.0	1	3	10	280.2 ± 17.2	0.25 ± 0.01	−24.8 ± 1.7	9.6 ± 2.3
*m*11	5	3.0	1	2	10	198.4 ± 17.8	0.29 ± 0.09	−24.7 ± 4.2	–
*m*12	5	3.0	1	3	10	147.2 ± 29.4	0.25 ± 0.02	−24.8 ± 1.7	–
*m*13	0.5	6.0	1	2	10	235.7 ± 31.2	0.30 ± 0.08	−25.3 ± 3.2	32.1 ± 1.5
*m*14	0.5	6.0	1	3	10	131.1 ± 20.2	0.28 ± 0.05	−35.2 ± 3.5	36.8 ± 3.2
*m*15	1	6.0	1	2	10	200.1 ± 21.7	0.30 ± 0.04	−28.9 ± 5.6	12.4 ± 1.2
m16	1	6.0	1	3	10	293.4 ± 8.9	0.31 ± 0.01	−26.9 ± 2.8	12.8 ± 3.0
*m*17	5	6.0	1	2	10	194.8 ± 8.8	0.38 ± 0.07	−28.9 ± 5.6	–
*m*18	5	6.0	1	3	10	383.4 ± 18.7	0.28 ± 0.05	−26.9 ± 2.8	–

D_H= hydrodynamic diameter. PDI = polydisperdity index. YP = yield of production

*b*DPPC@PLGA hNPs, as determined by the comparison of means of the quality attributes of the nanoparticles (i.e. size, PDI, zeta potential, and production yield). The absolute differences in attributes between microfluidic formulations (Fig. S1) were used to score their similarity to the benchtop control (%). *m*1 was identified as, on average, the most similar formulation (Fig. S2).

The resulting optimized hNPs (*m*1) exhibited a size of approximately 166 nm (± 19.9), very close to that of the benchtop formulation, with a

A

Formulation	PLGA % w/v	PVA:PLGA w:w	D_H nm ± SD	PDI mean ± SD	ζ potential mV ± SD	YP % ± SD
*b*DPPC@PLGA	1	-	159.7 ± 2.1	0.14 ± 0.02	-28.4 ± 2.4	54.5 ± 4.3
m1	0.5	-	166.5 ± 19.9	0.21 ± 0.08	-28.7 ± 5.9	37.1 ± 2.7
m1_PVA2	0.5	1:2	178.8 ± 4.0	0.11 ± 0.01	-28.2 ± 0.4	38.1 ± 1.2
m1_PVA4	0.5	1:4	205.1 ± 0.6	0.16 ± 0.01	-33.5 ± 4.0	30.8 ± 2.1
m1_PVA6	0.5	1:6	168.0 ± 3.7	0.15 ± 0.05	-35.8 ± 4.5	43.4 ± 2.6
m1_PVA8	0.5	1:8	162.7 ± 10.5	0.11 ± 0.02	-34.3 ± 3.1	42.6 ± 2.8

[a] D_H = hydrodynamic diameter. PDI = polydisperdity index. YP = yield of production.

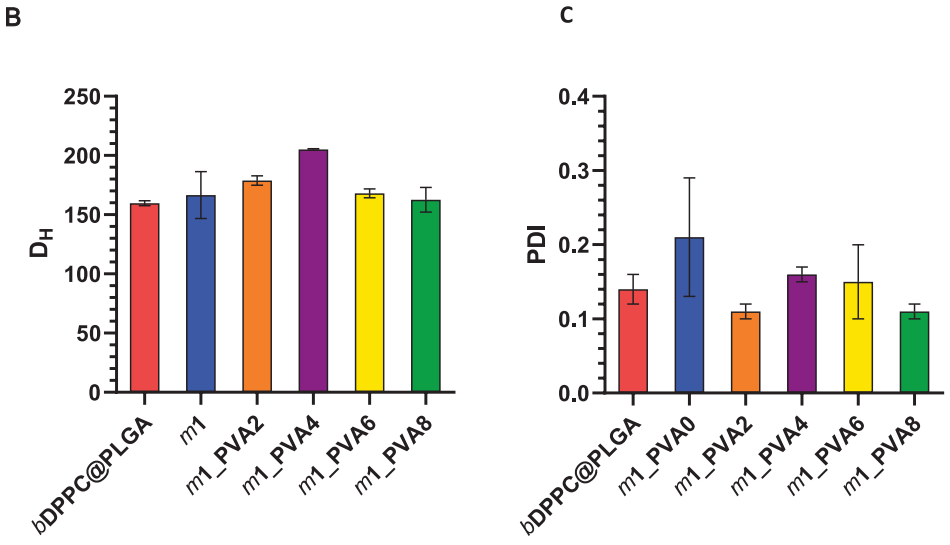

Fig. 3. (A) Effect of the PVA addition (w/w PVA: PLGA) on the colloidal properties of *m*DPPC@PLGA hNPs. Colloidal properties of *b*DPPC@PLGA and *m*1 DPPC@PLGA hNPs are reported for comparison. (B) Hydrodynamic diameter (D_H), (C) Polydispersity index (PDI). Results are reported as mean ± standard deviation (SD) from three independent batches (n = 3).

suitable PDI of around 0.2 and a quite good production yield of about 37 % ± 2.7 %. However, using only water as the diffusion phase resulted in unstable hNPs, which formed clearly visible precipitates within 24 h, even when stored at 4 °C (*Data not shown*). Given its role as an emulsion stabilizer (Costabile et al., 2024), the contribution of PVA 4–88 to the stability of the hNP dispersion was evaluated by adding it to the diffusion phase at various weight ratios relative to PLGA (0, 1:2, 1:4, 1:6, and 1:8 w/w) (Fig. 3A).

In general, the addition of PVA enhanced both the stability and quality of the *m*DPPC@PLGA hNPs (Figs. 3B and 3C). Notably, the highest production yields were observed for *m*1_PVA6 and *m*1_PVA8, which corresponded to the lowest PVA:PLGA ratios tested (Fig. 3A). The same systematic method for identifying the microfluidic formulation most similar to the benchtop control was likewise applied to the formulations produced with PVA (Fig. S3 and S4). Based on the comparative statistical analysis, *m*1_PVA8 was selected as the optimized protocol yielding *a* monodisperse population of *m*DPPC@PLGA hNPs with controlled size (<170 nm) and consistent zeta potential (–30 mV). The selected process condition shows a production yield of 43 %, which, if in general could be considered low to support scalability, at the same time is also inherently tight to the volume processed, and that can be addressed, for example, by increasing the volume processed, consequently reducing the impact of cutting tails. However, to obtain conclusive results, a follow-up study on how volumetric scale-up impacts the production yield of hNPs through microfluidics for siRNA encapsulation would be essential (Matthew et al., 2022; Webb et al., 2022).

A preliminary test was performed using a model non-targeting scrambled siRNA (siNC). As shown in Fig. S5A, *m*DPPC@PLGA hNPs loaded with siNC at a theoretical loading of 0.2 nmol *per* 10 mg of PLGA were successfully produced. Importantly, the incorporation of siRNA did not significantly affect key technological features of the hNPs, such as particle size, PDI, and ς potential, while maintaining an entrapment efficiency of approximately 50 % (Fig. S5A). The colloidal stability of the hNPs was preserved for up to 5 days when stored in water at 4 °C, as demonstrated in Fig. S5B.

Based on these encouraging results, the *m*1_PVA8 formulation was subsequently loaded with a therapeutically relevant siRNA pool targeting NF-κB p50 and p65 subunits (siNFκB). Two different loading levels were tested, that is 0.2 and 1 nmol *per* 10 mg of PLGA, corresponding to the formulations *m*DPPC@PLGA_siNFκB_0.2 and *m*DPPC@PLGA_siNFκB_1, respectively. The comprehensive characterization of *m*DPPC@PLGA_siNFκB formulations confirms the successful translation of the production process from conventional benchtop methods to a microfluidic-based platform (Fig. 4A). Notably, the microfluidically produced hNPs exhibit a D_H below 180 nm, along with a highly homogeneous size distribution, as evidenced by significantly lower PDI values compared to those *via* the benchtop method. However, the difference can be attributed to the working principles of DLS and NTA; DLS provides an intensity-weighted average, often skewed by larger particles or aggregates, while NTA gives a number-weighted distribution (Tian et al., 2024). Minor variations in sample handling and sensitivity to polydispersity may also contribute (Tian et al., 2024). These findings are further supported by high-resolution transmission electron microscopy (TEM) images, which show that both *b*DPPC@PLGA_siNFkB hNPs and *m*DPPC@PLGA_siNFkB hNPs (Fig. 4B) exhibit a uniform population of spherically shaped nanoparticles, thereby confirming the consistency of morphology irrespective of the production technique. Finally, *m*DPPC@PLGA hNPs effectively encapsulated high amounts of siNFkB, showing actual loadings of 2.8 ± 1.4 nmol/100 mg and 15.7 ± 6.2 nmol/100 mg for *m*DPPC@PLGA_NFkB_0.2 and *m*DPPC@PLGA_NFkB_1 hNPs,

A

	Theoretical Loading (nmol/10 mg)	DLS			NTA			YP (% ± SD)	AL[b] (nmol / 100 mg hNPs)
		D_H nm ± SD	PDI mean ±SD	ζ potential mV ± SD	Mean ± SD	SPAN ± SD	[hNPs/mL]		
*b*DPPC@PLGA_siNFkB	0.2	177.6 ± 9.2	0.19 ± 0.04	-28.1 ± 1.6	143.8 ± 6.9	1.2 ± 0.05	$4.6*10^{11}$	56.4 ± 6.1	2.5 ± 0.1
*m*DPPC@PLGA_siNFkB	0.2	178.1 ± 9.8	0.14 ± 0.03	-29.0 ± 2.8	168.9 ± 5.4	1.1 ± 0.09	$3.5*10^{11}$	36.6 ± 3.7	2.8 ± 1.4
*b*DPPC@PLGA_siNFkB	1	169.5 ± 7.4	0.16 ± 0.09	-32.4 ± 2.5	154.5 ± 5.3	1.0 ± 0.06	$3.9*10^{11}$	58.2 ± 5.8	14.0 ± 1.2
*m*DPPC@PLGA_siNFkB	1	155.3 ± 10.8	0.15 ± 0.01	-31.7 ± 1.2	142.5 ± 4.1	0.9 ± 0.08	$2.9*10^{11}$	37.4 ± 4.2	15.7 ± 6.2

[a] D_H = hydrodynamic diameter. PDI = polydisperdity index. YP = yield of production.
[b] *The a*ctual loading is expressed as nmol of encapsulated siRNA per 100 mg of *mDPPC@PLG*Ahnps based on the yields of production

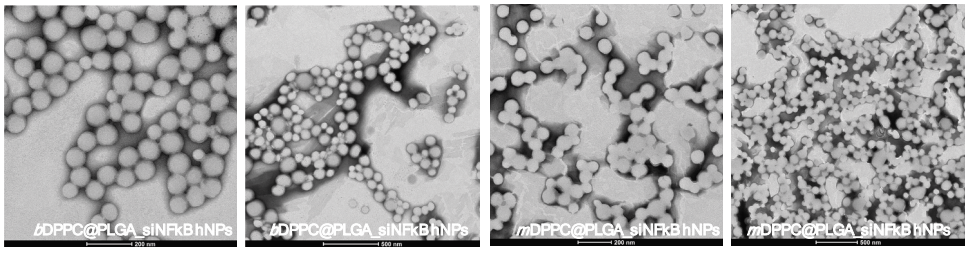

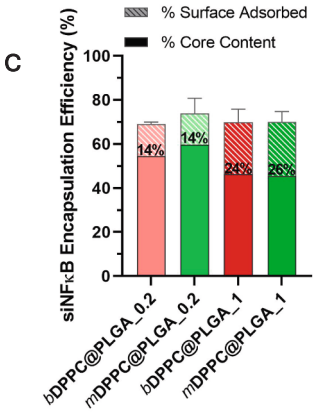

Fig. 4. (A) Effect of siNFkB loading on the colloidal properties of *m*DPPC@PLGA hNPs. The hydrodynamic diameter (D_H) and ζ potential are measured by Zetasizer Nano ZS. Results are reported as mean ± standard deviation (SD) from three independent batches (n = 3). Mean, Span, and Particle concentration (hNPs/mL) as calculated by the Nanosight Pro software. (B) TEM images of *b*DPPC@PLGA_siNFkB hNPs and *m*DPPC@PLGA_siNFkB hNPs. The field is representative of formulations. (C) Encapsulation efficacy (%) including both core-encapsulated and surface-adsorbed fractions.

respectively.

To gain a better understanding of the amount of siRNA adsorbed on the surface in comparison to the amount of siRNA effectively encapsulated and protected within the PLGA core, the detachment of siRNA from the surface of the hNPs was induced through a heparin displacement procedure followed by analytical quantification. This highly negatively charged polysaccharide competitively occupies siRNA binding sites on the hNP surface (Vader et al., 2012).

The distribution of siNFkB within the structure of the hNPs is shown in Fig. 4C and in Table S2. As shown, the overall encapsulation efficiency of siNFkB within the hNPs when produced by either method remains almost comparable, showing only a slight increase in the *m*DPPC@PLGA hNPs for both loading levels compared to *b*DPPC@PLGAs hNPs produced by the conventional method. However, the higher the theoretical loading, the lower the percentage of siRNA entrapped in the core (i.e., the higher the percentage adsorbed on the surface of the hNPs). This is not surprising, considering that all the components of the *m*DPPC@PLGA hNPs, which meet at the flow focusing point, interact under the pressure of the laminar flow, leading to a higher siRNA distribution on the surface (Cózar-Bernal et al., 2011; Rezvantalab and Keshavarz Moraveji, 2019).

3.2. In vitro release studies

In vitro release kinetics were evaluated to determine how microfluidic production affects the release profile of encapsulated siNFκB. As illustrated in Fig. 5, both *b*DPPC@PLGA and *m*DPPC@PLGA hNPs exhibit a biphasic release pattern. The initial burst corresponds to the rapid release of siRNA adsorbed on the nanoparticle surface, while the second phase reflects the sustained diffusion of siRNA through the PLGA matrix. At both tested siRNA loadings, *m*DPPC@PLGA hNPs released less siRNA over 14 days, with *b*DPPC@PLGA hNPs reaching approximately 50 % release in the same period. Notably, *m*DPPC@PLGA hNPs exhibit consistently lower cumulative siNFκB release than *b*DPPC@PLGA.

In all cases, we observe differences in release kinetics during the first 5 h compared to timepoints after 24 h. Because this two-step release phenomenon was consistent across all formulations, a model was fit in two segments (Fig. S6). The Baker-Lonsdale model was employed to describe release from a spherical matrix (Rasool et al., 2020; Strategies to Modify the Drug Release from Pharmaceutical Systems, 2015). Here, the fraction of payload released is a function of time (Eq. 4):

$$f\left(\frac{M_t}{M_\infty}\right) = \frac{3}{2}\left[1 - \left(1 - \frac{M_t}{M_\infty}\right)^{2/3}\right] - \frac{M_t}{M_\infty} = Kt$$

The ordinate axis represents a function $f(M_t/M_\infty)$, determined for each point of the release curve and plotted as a linearized relationship *versus* time (*t*), which is related by the release constant *K*. Here we make the assumptions that the particles are spherical and monodisperse, with a continuous composition, and the release of our payload has a constant diffusivity. We further assume perfect *sink* conditions and a uniform distribution of payload within our matrix. The inset in Fig. S6 A shows a magnified section of the release with the Baker-Lonsdale model fit to the first 5 h. The model does not fit the siRNA release profile as well as it should, as shown in Table S1. This indicates that the initial release is not described by simple diffusion and is likely mediated by burst-release effects or localized phenomena of siRNA at or near the hNP surface. However, the Baker-Lonsdale models show good agreement with the release profiles after 24 hr (R^2 values between 0.981 and 0.995) (Table S3). Furthermore, the residuals for the Baker-Lonsdale model are randomly distributed about 0, indicating that this model sufficiently describes the diffusion-based release from the spherical system (Fig. S6B). Proceeding with the Baker-Lonsdale model, *b*DPPC@PLGA hNPs release siRNA more rapidly compared to *m*DPPC@PLGA hNPs and likewise lose a more significant fraction of initial siRNA during the burst phase. Furthermore, it does not appear that initial siRNA load has a strong effect on release kinetics.

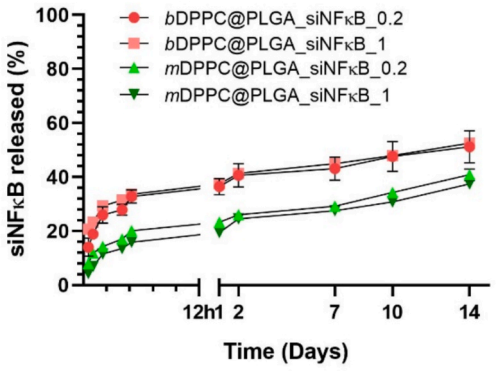

Fig. 5. *In vitro* release kinetics of siNFκB from *b*DPPC@PLGA and *m*DPPC@PLGA hNPs in PBS (pH 7.4) at different siRNA loadings. Data are presented as cumulative siRNA release (%) over time, expressed as mean ± SD (n = 3).

Overall, consistent with previous findings (Karnik et al., 2008; Rezvantalab and Keshavarz Moraveji, 2019; Shepherd et al., 2021), results suggest that microfluidic synthesis yields a more compact, possibly denser nanoparticle structure. The structural refinement enabled by microfluidics results in a slower, more controlled release, retaining the extended-release benefits of the PLGA core.

3.3. Structural characterization of siRNA-loaded mDPPC@PLGA hNPs

Differential Scanning Calorimetry (DSC) thermograms offer valuable insights into changes in component interactions within hNPs formulations. These changes may influence the thermal behaviour and reveal differences in molecular interactions among formulation constituents —including PLGA, DPPC, and siRNA—depending on the DPPC@PLGA hNP production method, whether using conventional bench-scale techniques or microfluidics (Fig. 6A). Table S4 provides DSC data for all nanoparticle subgroups reporting both glass transition temperatures (Tg, °C) and enthalpy values (J/g).

PLGA shows a broad endothermic glass transition at T_g 38.5 °C (1.86 J/g) without sharp peaks, characteristic of its amorphous nature (Liu and McEnnis, 2022). DPPC, on the other hand, exhibits a well-defined phase transition peak at 62.5 °C (48.8 J/g), characteristic of its main phase transition (gel to liquid-crystalline phase) (Cevc and Marsh, 1985; Garvey et al., 2023). Notably, both bench-formulated and microfluidically prepared hNPs show distinct thermal profiles compared to raw materials. *b*DPPC@PLGA_NFκB hNPs exhibit a T_1 transition at 40.1 °C with an enthalpy of 1.09 J/g, and a T_2 transition at 57.7 °C (2.32 J/g). In contrast, *m*DPPC@PLGA_siNFκB hNPs show a T_1 transition at 44.0 °C with an enthalpy of 4.61 J/g, along with a minor event at 61.5 °C (0.94 J/g). These quantitative differences, together with the observed thermal shifts, underscore the influence of the production method on the molecular organization within the nanoparticles. The upward shift of *Tg* in the microfluidic formulation indicates stronger molecular interactions among the components and reduced polymer chain mobility, likely arising from the more homogeneous mixing and rapid solvent exchange characteristic of microfluidic processing. Conversely, hNPs prepared by the benchtop method display less uniform molecular mixing and greater lipid phase separation.

Overall, thermal shifts and peak broadening observed in both nanoparticle systems confirm successful encapsulation and molecular interactions among PLGA, DPPC, and siRNA. Notably, the microfluidic approach outperforms the benchtop method by promoting more uniform particle formation and tighter component integration, as evidenced by clearer thermal profiles and the reduction of residual free DPPC peaks. These findings further support the enhanced structural

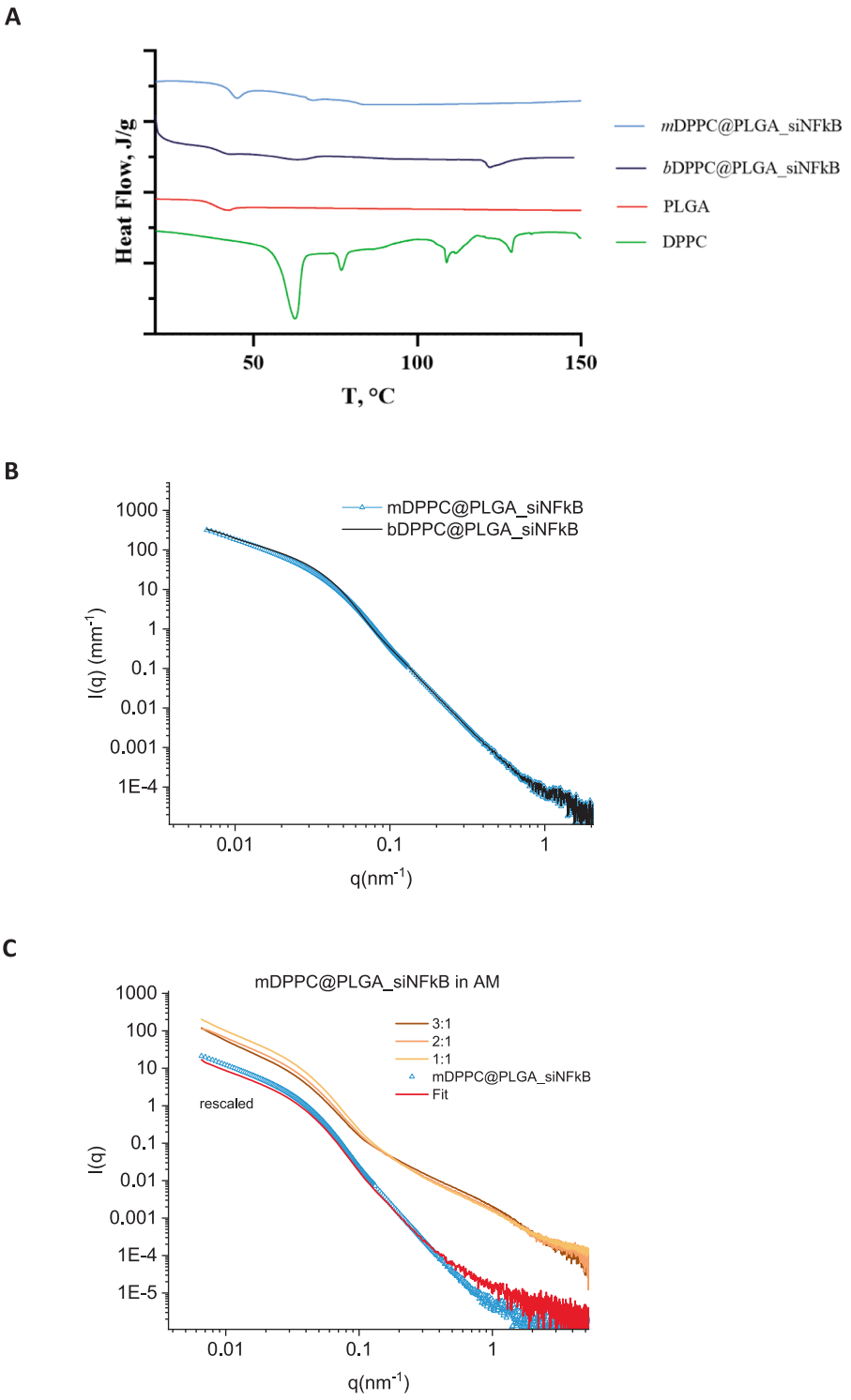

Fig. 6. Structural characterization of *m*DPPC@PLGA hNPs. A) DSC thermograms of *m*DPPC@PLGA_siNFkB hNPs compared to the *b*DPPC@PLGA_siNFkB hNPs. The heat flows are normalized. The endothermic peaks are downwards. B) SAXS profiles of *m*DPPC@PLGA_siNFkB (light blue) and *b*DPPC@PLGA_siNFkB (black) after intensity renormalization by a yield% factor of 0.4. C) SAXS profiles of the mixtures of *m*DPPC@PLGA_siNFkB and AM at three different volume ratios (brown, orange, and yellow lines) and a comparison of the reconstructed profile of the *m*DPPC@PLGA_siNFkB inside AM (red) with the profile in water (light blue), both rescaled for clarity.

refinement of microfluidically produced hNPs, consistent with their slower and more controlled release of siRNA.

To deepen the study of the structural features of the hNPs prepared either by microfluidics or the standard benchtop procedure, SAXS was applied to *m*DPPC@PLGA_siNFkB and *b*DPPC@PLGA_siNFkB stabilized by PVA 4_88. Fig. 6B reports the SAXS scattering profile I(q) of the hNP dispersions in water. For comparison, a normalization of I(q) by the corresponding yield % was applied. The normalization of the intensity indicates that the microfluidic yield is 0.4-fold that of the standard method. Results show that the profiles largely overlap, highlighting the effectiveness of the microfluidic setup in generating hNPs with size and shape comparable to the standard ones. Best fit of the data was obtained

by applying a model of interacting spherical particles (Kotlarchyk and Chen, 1983; Menon et al., 1991). In the intermediate-to-high q range ($0.04\ nm^{-1} < q < 0.8\ nm^{-1}$), the SAXS intensity decreases following a q^{-4} power law, consistent with smooth particle surfaces. Lowest q profiles (in the range of particles overall size) increase, showing some hNP adhesion. The applied model fitted a geometrical radius of 68 ± 0.3 nm (PDI 0.2) and 64 ± 0.0.4 nm (PDI 0.2) for *b*DPPC@PLGA_siNFkB and *m*DPPC@PLGA_siNFkB, respectively, and the strongest attraction among the microfluidic ones. As expected, DLS hydrodynamic radii are slightly larger. Though a direct comparison with the DLS data is not possible, since the SAXS data were acquired at much higher concentrations, TEM images confirm some particles aggregation in the samples.

Another aspect that requires further investigation is the addition, even if only as a colloidal stabilizer, of PVA 4–88 (Costabile et al., 2024). Recent studies have unveiled the crucial role of PVA molecular weight and hydrolysis grade in the production of mucus-penetrating PLGA nanoparticles (Savadi et al., 2025). The interaction that *m*DPPC@PLGA hNPs establish with mucin, the primary mucus component, was evaluated using combined UV–Vis/DLS analyses, as described in a previous study (Conte et al., 2022). Results suggest neither hNP aggregation nor protein surface absorption in the presence of 0.08 % w/v mucin (Fig. S7).

SAXS analysis was further applied to investigate the stability of the formulation in an artificial mucus solution. Aqueous dispersions of hNPs were prepared at three different volume ratios to artificial mucus (1:1, 2:1, and 3:1). In line with results achieved with previously developed siRNA-loaded hNPs surface-engineered with DPPC (Conte et al., 2022; d'Angelo et al., 2018), Fig. 6C shows that *m*DPPC@PLGA_siNFkB hNPs are stable after incubation in mucus for a few hours, as the reconstructed spectra (red line) obtained by subtraction of AM spectrum from the mixed system spectrum, corresponds to the one measured in water (light blue symbols).

3.4. Silencing of NF-κB expression via siRNA delivery using microfluidic and Benchtop-Formulated DPPC@PLGA hNPs

To evaluate the cytosolic release of siRNA, preliminary cytotoxicity was carried out on A549 cells after incubation with both *m*DPPC@PLGA hNPs and *b*DPPC@PLGA hNPs, confirming their tolerability (Fig. S8). The ability of *b*DPPC@PLGA hNPs to downregulate NF-κB expression has been previously demonstrated (Conte et al., 2022) and served as the experimental frame of reference in this experiments. The NF-κB p65 (RelA) subunit is a key transcription factor that plays a central role in inflammation. Its prolonged or aberrant activation is implicated in various chronic diseases, indicating p65 as a significant target for therapeutic intervention in lung inflammatory processes. LPS stimulation markedly increased the expression of the NF-κB p65 subunit, that is central to regulating inflammation, in A549 cells compared to CTR, confirming the effective activation of the NF-κB pathway (°p < 0.05; Fig. 7). *m*DPPC@PLGA_siNFkB hNPs led to a significant reduction in NF-κB levels (**p < 0.01 vs. LPS, Fig. 7), demonstrating the efficiency of the intracellular delivery and the functional silencing ability. A similar profile was observed after *b*DPPC@PLGA_siNFκB hNPs treatment (*p < 0.05 vs. LPS, Fig. 7). Transfection with siNFκB using lipofectamine complexes effectively suppressed NFκB expression in LPS-stimulated cells, validating the specificity and efficiency of siRNA-mediated silencing (*p < 0.05 vs. LPS, Fig. 7).

4. Conclusion

In this work, we first demonstrate the successful adaptation of an established benchtop emulsion-solvent diffusion protocol for producing Lipid@PLGA hybrid nanoparticles to a commercially accessible microfluidic platform using a double-chip-in-series configuration. Through a systematic investigation of chip coatings, geometries, processing conditions, and formulation parameters, we optimized the microfluidic process to yield hNPs with core–shell architecture and quality attributes closely matching those of hNPs produced by conventional methods. Notably, thermodynamic analysis revealed a more refined amorphous structure in the microfluidic hNPs compared to the benchtop reference, thereby further improving control over siRNA release kinetics. Effective siRNA encapsulation and preserved molecular integrity were confirmed *via* functional *in vitro* silencing of the NF-κB pathway in human lung epithelial cells. These results collectively validate the technological translation of the emulsion–solvent diffusion method from bulk-scale to continuous microfluidic production, highlighting its potential for scalable, reproducible, and clinically relevant RNA delivery systems.

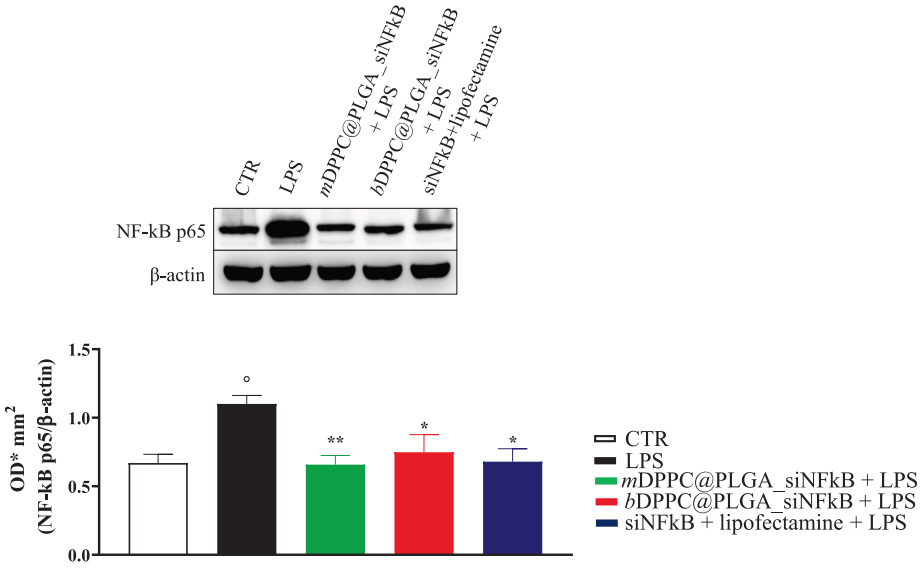

Fig. 7. Representative Western blotting for NF-κB p65 in protein extracts of A549 cells. A549 cells were treated with a *b*DPPC@PLGA hNPs or *m*DPPC@PLGA hNPs (0.2 mg/mL) loaded with 40 nM of siRNA targeting NF-κB (siNFκB) and kept at 37 °C in a humidified atmosphere containing 5 % CO_2. An equal amount of siNFκB/lipofectamine complexes was used for validation. At 42 h, cells were stimulated with lipopolysaccharide (LPS, 10 μg/mL) to induce NF-κB expression, and the assay was stopped at 48 h.

6. Consent for publication

Not applicable since the study did not include humans.

CRediT authorship contribution statement

Ersilia Villano: Writing – original draft, Investigation, Data curation. **Teresa Silvestri:** Writing – original draft, Investigation, Data curation. **Susy Brusco:** Investigation, Data curation. **Erika Esposito:** Writing – original draft, Investigation. **Chiara Infolfi:** Investigation, Data curation. **Thomas L. Moore:** Writing – original draft, Formal analysis. **Emma Mitidieri:** Writing – review & editing, Methodology, Data curation. **Raffaella Sorrentino:** Writing – review & editing, Resources. **Fabiana Quaglia:** Writing – review & editing, Resources. **Paola Brocca:** Writing – review & editing, Investigation, Data curation. **Ivana d'Angelo:** Writing – review & editing, Methodology. **Roberta d'Emmanuele di Villa Bianca:** Writing – review & editing, Methodology, Conceptualization. **Gabriella Costabile:** Writing – review & editing, Methodology, Data curation, Conceptualization. **Francesca Ungaro:** Writing – review & editing, Funding acquisition, Data curation, Conceptualization.

5. Ethics approval and consent to participate

Not applicable since the study did not include animals or humans.

Declaration of competing interest

The authors declare that they have no known competing financial interests or personal relationships that could have appeared to influence the work reported in this paper.

Acknowledgements

The authors acknowledge the grant CN00000041 "National Center for Gene Therapy and Drugs based on RNA Technology" (concession number 1035 of 17 June 2022-PNRR MUR - M4C2 - Investment 1.4 Call "National Centers", funded by EU- NextGenerationEU), code project (CUP: E63C22000940007).

The authors thank Dr Antonella Giarra at Department of Chemical Sciences, University of Naples Federico II, for technical support in TEM analysis. The authors acknowledge the ID02 beamline staff for their technical support and the ESRF for providing beamtime and facilities.

Appendix A. Supplementary data

Supplementary data to this article can be found online at https://doi.org/10.1016/j.ijpharm.2025.126440.

Data availability

The datasets generated during and/or analyzed during the current study are available from the corresponding author on reasonable request.

References

Breßler, I., Kohlbrecher, J., Thünemann, A.F., 2015. *SASfit* : a tool for small-angle scattering data analysis using a library of analytical expressions. J. Appl. Cryst. 48, 1587–1598. https://doi.org/10.1107/S1600576715016544.

Brusco, S., Conte, G., Corteggio, A., Silvestri, T., Spitaleri, A., Brocca, P., Miro, A., Quaglia, F., d'Angelo, I., D'Apice, L., Italiani, P., Costabile, G., Ungaro, F., 2024. PEI-Engineered Lipid@PLGA hybrid nanoparticles for multimodal delivery of antigens and immune adjuvants to the respiratory mucosa. Adv Healthcare Materials 2402688. https://doi.org/10.1002/adhm.202402688.

Cevc, G., Marsh, D., 1985. Hydration of noncharged lipid bilayer membranes. Theory and experiments with phosphatidylethanolamines. Biophys. J . 47, 21–31. https://doi.org/10.1016/S0006-3495(85)83872-8.

Comegna, M., Conte, G., Falanga, A.P., Marzano, M., Cernera, G., Di Lullo, A.M., Amato, F., Borbone, N., D'Errico, S., Ungaro, F., d'Angelo, I., Oliviero, G., Castaldo, G., 2021. Assisting PNA transport through cystic fibrosis human airway epithelia with biodegradable hybrid lipid-polymer nanoparticles. Sci. Rep. 11. https://doi.org/10.1038/s41598-021-85549-z.

Conte, G., Costabile, G., Baldassi, D., Rondelli, V., Bassi, R., Colombo, D., Linardos, G., Fiscarelli, E.V., Sorrentino, R., Miro, A., Quaglia, F., Brocca, P., d'Angelo, I., Merkel, O.M., Ungaro, F., 2022. Hybrid lipid/polymer nanoparticles to tackle the cystic fibrosis mucus barrier in siRNA delivery to the lungs: does PEGylation make the difference? ACS Appl. Mater. Interfaces 14, 7565–7578. https://doi.org/10.1021/acsami.1c14975.

Costabile, G., Baldassi, D., Müller, C., Groß, B., Ungaro, F., Schubert, S., Firestine, S.M., Merkel, O.M., 2024. Antibiotic-loaded nanoparticles for the treatment of intracellular methicillin-resistant Staphylococcus Aureus infections: In vitro and in vivo efficacy of a novel antibiotic. J. Control. Release 374, 454–465. https://doi.org/10.1016/j.jconrel.2024.08.029.

Costabile, G., d'Angelo, I., Rampioni, G., Bondì, R., Pompili, B., Ascenzioni, F., Mitidieri, E., di Villa, D., Bianca, R., Sorrentino, R., Miro, A., Quaglia, F., Imperi, F., Leoni, L., Ungaro, F., 2015. Toward Repositioning Niclosamide for Antivirulence Therapy of *Pseudomonas aeruginosa* Lung Infections: Development of Inhalable Formulations through Nanosuspension Technology. Mol. Pharm. 12, 2604–2617. https://doi.org/10.1021/acs.molpharmaceut.5b00098.

Cózar-Bernal, M.J., Holgado, M.A., Arias, J.L., Muñoz-Rubio, I., Martín-Banderas, L., Álvarez-Fuentes, J., Fernández-Arévalo, M., 2011. Insulin-loaded PLGA microparticles: flow focusing *versus* double emulsion/solvent evaporation. J. Microencapsul. 28, 430–441. https://doi.org/10.3109/02652048.2011.576786.

d'Angelo, I., Costabile, G., Durantie, E., Brocca, P., Rondelli, V., Russo, A., Russo, G., Miro, A., Quaglia, F., Petri-Fink, A., Rothen-Rutishauser, B., Ungaro, F., 2018. Hybrid Lipid/polymer nanoparticles for pulmonary delivery of siRNA: development and fate upon *In Vitro* deposition on the human epithelial airway barrier. J. Aerosol Med. Pulm. Drug Deliv. 31, 170–181. https://doi.org/10.1089/jamp.2017.1364.

Di Villa Bianca, R., d'Emmanuele, C., C., Mitidieri, E., De Dominicis, G., Rossi, A., Sautebin, L., Cirino, G., Bucci, M., Sorrentino, R., 2010. Hydrogen sulphide induces mouse paw oedema through activation of phospholipase A_2. British J Pharmacology 161, 1835–1842. https://doi.org/10.1111/j.1476-5381.2010.01016.x.

Esposito, E., Indolfi, C., Bello, I., Smimmo, M., Vellecco, V., Schettino, A., Montanaro, R., Morroni, F., Sita, G., Graziosi, A., Panza, E., Sorrentino, R., Di Villa, D., Bianca, R., Mitidieri, E., 2024. The endocrine disruptor vinclozolin causes endothelial injury via eNOS/Nox4/IRE1α signaling. Eur. J. Pharmacol. 977, 176758. https://doi.org/10.1016/j.ejphar.2024.176758.

Garvey, C.J., Bryant, S.J., Elbourne, A., Hunt, T., Kent, B., Kreuzer, M., Strobl, M., Steitz, R., Bryant, G., 2023. Phase separation in a ternary DPPC/DOPC/POPC system with reducing hydration. J. Colloid Interface Sci. 638, 719–732. https://doi.org/10.1016/j.jcis.2023.01.145.

Germain, M., Caputo, F., Metcalfe, S., Tosi, G., Spring, K., Åslund, A.K.O., Pottier, A., Schiffelers, R., Ceccaldi, A., Schmid, R., 2020. Delivering the power of nanomedicine to patients today. J. Control. Release 326, 164–171. https://doi.org/10.1016/j.jconrel.2020.07.007.

Hernández-Giottonini, K.Y., Rodríguez-Córdova, R.J., Gutiérrez-Valenzuela, C.A., Peñuñuri-Miranda, O., Zavala-Rivera, P., Guerrero-Germán, P., Lucero-Acuña, A., 2020. PLGA nanoparticle preparations by emulsification and nanoprecipitation techniques: effects of formulation parameters. RSC Adv. 10, 4218–4231. https://doi.org/10.1039/C9RA10857B.

Joyce, P., Allen, C.J., Alonso, M.J., Ashford, M., Bradbury, M.S., Germain, M., Kavallaris, M., Langer, R., Lammers, T., Peracchia, M.T., Popat, A., Prestidge, C.A., Rijcken, C.J.F., Sarmento, B., Schmid, R.B., Schroeder, A., Subramaniam, S., Thorn, C.R., Whitehead, K.A., Zhao, C.-X., Santos, H.A., 2024. A translational framework to DELIVER nanomedicines to the clinic. Nat. Nanotechnol. 19, 1597–1611. https://doi.org/10.1038/s41565-024-01754-7.

Karnik, R., Gu, F., Basto, P., Cannizzaro, C., Dean, L., Kyei-Manu, W., Langer, R., Farokhzad, O.C., 2008. Microfluidic platform for controlled synthesis of polymeric nanoparticles. Nano Lett. 8, 2906–2912. https://doi.org/10.1021/nl801736q.

Kotlarchyk, M., Chen, S.-H., 1983. Analysis of small angle neutron scattering spectra from polydisperse interacting colloids. J. Chem. Phys. 79, 2461–2469. https://doi.org/10.1063/1.446055.

Kronenfeld, J.M., Rother, L., Saccone, M.A., Dulay, M.T., DeSimone, J.M., 2024. Roll-to-roll, high-resolution 3D printing of shape-specific particles. Nature 627, 306–312. https://doi.org/10.1038/s41586-024-07061-4.

Li, S., Yang, B., Ye, L., Hu, S., Li, B., Yang, Y., Hu, Y., Jia, X., Feng, L., Xiong, Z., 2025. Multistage microfluidic assisted Co-delivery platform for dual-agent facile sequential encapsulation. Eur. J. Pharm. Biopharm. 207, 114616. https://doi.org/10.1016/j.ejpb.2024.114616.

Liu, G., McEnnis, K., 2022. Glass transition Temperature of PLGA Particles and the Influence on Drug delivery applications. Polymers 14, 993. https://doi.org/10.3390/polym14050993.

Liu, M., Wang, Y., Zhang, Y., Hu, D., Tang, L., Zhou, B., Yang, L., 2025a. Landscape of small nucleic acid therapeutics: moving from the bench to the clinic as next-generation medicines. Sig Transduct Target Ther 10. https://doi.org/10.1038/s41392-024-02112-8.

Liu, M., Wang, Y., Zhang, Y., Hu, D., Tang, L., Zhou, B., Yang, L., 2025b. Landscape of small nucleic acid therapeutics: moving from the bench to the clinic as next-generation medicines. Sig Transduct Target Ther 10, 73. https://doi.org/10.1038/s41392-024-02112-8.

Matthew, S.A.L., Rezwan, R., Perrie, Y., Seib, F.P., 2022. Volumetric Scalability of Microfluidic and Semi-batch Silk Nanoprecipitation Methods. Molecules 27, 2368. https://doi.org/10.3390/molecules27072368.

Menon, S.V.G., Manohar, C., Rao, K.S., 1991. A new interpretation of the sticky hard sphere model. J. Chem. Phys. 95, 9186–9190. https://doi.org/10.1063/1.461199.
Michael, S., 2021. SAXSutilities2: a graphical user interface for processing and analysis of Small-Angle X-ray Scattering data. https://doi.org/10.5281/ZENODO.5825707.
Rasool, A., Ata, S., Islam, A., Rizwan, M., Azeem, M.K., Mehmood, A., Khan, R.U., Qureshi, A.U.R., Mahmood, H.A., 2020. Kinetics and controlled release of lidocaine from novel carrageenan and alginate-based blend hydrogels. Int. J. Biol. Macromol. 147, 67–78. https://doi.org/10.1016/j.ijbiomac.2020.01.073.
Rezvantalab, S., Keshavarz Moraveji, M., 2019. Microfluidic assisted synthesis of PLGA drug delivery systems. RSC Adv. 9, 2055–2072. https://doi.org/10.1039/C8RA08972H.
Roces, C.B., Christensen, D., Perrie, Y., 2020. Translating the fabrication of protein-loaded poly(lactic-co-glycolic acid) nanoparticles from bench to scale-independent production using microfluidics. Drug Deliv. and Transl. Res. 10, 582–593. https://doi.org/10.1007/s13346-019-00699-y.
Savadi, P., Casale, A., Roggia, M., Conte, G., Lozano, M.V., Costabile, G., Ungaro, F., Cosconati, S., Santander-Ortega, M., d'Angelo, I., 2025. Unveiling the role of poly (vinyl alcohol) in the production of mucus-penetrating PLGA nanoparticles. Int. J. Pharm. 673, 125398. https://doi.org/10.1016/j.ijpharm.2025.125398.
Schiller, S., Hanefeld, A., Schneider, M., Lehr, C.-M., 2020. Towards a Continuous Manufacturing Process of Protein-Loaded Polymeric Nanoparticle Powders. AAPS PharmSciTech 21, 269. https://doi.org/10.1208/s12249-020-01814-w.
Schiller, S., Hanefeld, A., Schneider, M., Lehr, C.-M., 2015. Focused Ultrasound as a Scalable and Contact-Free Method to Manufacture Protein-Loaded PLGA Nanoparticles. Pharm. Res. 32, 2995–3006. https://doi.org/10.1007/s11095-015-1681-7.
Shepherd, S.J., Issadore, D., Mitchell, M.J., 2021. Microfluidic formulation of nanoparticles for biomedical applications. Biomaterials 274, 120826. https://doi.org/10.1016/j.biomaterials.2021.120826.
Strategies to Modify the Drug Release from Pharmaceutical Systems, 2015. . Elsevier. https://doi.org/10.1016/C2014-0-02342-8.
Sun, X., Setrerrahmane, S., Li, C., Hu, J., Xu, H., 2024. Nucleic acid drugs: recent progress and future perspectives. Sig Transduct Target Ther 9. https://doi.org/10.1038/s41392-024-02035-4.
Tian, Y., Tian, D., Peng, X., Qiu, H., 2024. Critical parameters to standardize the size and concentration determination of nanomaterials by nanoparticle tracking analysis. Int. J. Pharm. 656, 124097. https://doi.org/10.1016/j.ijpharm.2024.124097.
Unchained Labs, 2024. Microfluidic Production of 20 to 50 μm Core-Shell PLGA Beads.
Vader, P., Van Der Aa, L.J., Engbersen, J.F.J., Storm, G., Schiffelers, R.M., 2012. Physicochemical and Biological Evaluation of siRNA Polyplexes based on PEGylated Poly(amido amine)s. Pharm. Res. 29, 352–361. https://doi.org/10.1007/s11095-011-0545-z.
Wadhwa, A., Bobak, T.R., Bohrmann, L., Geczy, R., Sekar, S., Sathyanarayanan, G., Kutter, J.P., Franzyk, H., Foged, C., Saatchi, K., Häfeli, U.O., 2023. Pulmonary delivery of siRNA-loaded lipid-polymer hybrid nanoparticles: effect of nanoparticle size. OpenNano 13, 100180. https://doi.org/10.1016/j.onano.2023.100180.
Wang, J., Song, Y., 2017. Microfluidic Synthesis of Nanohybrids. Small 13, 1604084. https://doi.org/10.1002/smll.201604084.
Wang, S., Weissman, D., Dong, Y., 2025. RNA chemistry and therapeutics. Nat. Rev. Drug Discov. https://doi.org/10.1038/s41573-025-01237-x.
Webb, C., Ip, S., Bathula, N.V., Popova, P., Soriano, S.K.V., Ly, H.H., Eryilmaz, B., Nguyen Huu, V.A., Broadhead, R., Rabel, M., Villamagna, I., Abraham, S., Raeesi, V., Thomas, A., Clarke, S., Ramsay, E.C., Perrie, Y., Blakney, A.K., 2022. Current Status and Future Perspectives on MRNA Drug Manufacturing. Mol. Pharm. 19, 1047–1058. https://doi.org/10.1021/acs.molpharmaceut.2c00010.
Zander, A.J., Ehrlich, M.-S., Rehman, S.U., Schneider, M., 2025. Evaporation-triggered nanoprecipitation for PLGA nanoparticle formation using a spinning-disc system. J. Drug Delivery Sci. Technol. 108, 106901. https://doi.org/10.1016/j.jddst.2025.106901.
Zhang, X., Chan, H.W., Shao, Z., Wang, Q., Chow, S., Chow, S.F., 2025. Navigating translational research in nanomedicine: a strategic guide to formulation and manufacturing. Int. J. Pharm. 671, 125202. https://doi.org/10.1016/j.ijpharm.2025.125202.